Journal of Photochemistry and Photobiology 9 (2022) 100090

Contents lists available at ScienceDirect

Journal of Photochemistry and Photobiology

journal homepage: www.sciencedirect.com/journal/journal-of-photochemistry-and-photobiology

Photocatalyst assemblies with two halide ions

Michael D. Turlington, Alexander M. Deetz, Dylan Vitt, Gerald J. Meyer *

Department of Chemistry, University of North Carolina at Chapel Hill, Murray Hall 2202B, Chapel Hill, NC 27599-3290, United States

A B S T R A C T

A series of ruthenium polypyridyl photocatalysts bearing amide functional groups were designed that successfully promoted halide assembly in CH_2Cl_2 and CH_3CN solution. In CH_2Cl_2, halide assembly was accompanied by a visible color change, and the spectral changes presented clear evidence for two halide binding events, yielding a 1:2 ruthenium:halide assembly. In the more polar solvent CH_3CN, 1:2 assembly structures were also observed with chloride, bromide, and iodide, and large equilibrium constants were measured for association of the first and second halide ($K_{11} = 0.04 - 2 \times 10^6\ M^{-1}$, $K_{12} = 0.01 - 3 \times 10^5\ M^{-1}$). Varying the functional groups on the ancillary ligands tuned the excited-state reduction potentials ($Ru^{2+*/+}$), resulting in a photocatalyst capable of performing iodide oxidation. Quenching of the photocatalyst excited state resulted in static and dynamic quenching, and a Stern-Volmer analysis yielded two linear regions at low and high iodide concentrations. The dynamic quenching rate constants ($k_q = 6.8$ and $4.0 \times 10^{10}\ M^{-1}\ s^{-1}$) and static quenching constants ($K_S = 2.4$ and $0.13 \times 10^4\ M^{-1}$) at low and high iodide concentrations, respectively, were consistent with dynamic quenching of Ru^{2+} and $[Ru^{2+},I^-]^+$, and static quenching of $[Ru^{2+},I^-]^+$and $[Ru^{2+},2I^-]$. Transient absorption spectroscopy revealed that the quenching reaction yielded a reduced ruthenium (Ru^+) as the primary photoproduct and diiodide ($I_2^{\bullet -}$) as a secondary photoproduct. The second-order rate constant for $I_2^{\bullet -}$ formation was measured to be $2.5 \times 10^{10}\ M^{-1}\ s^{-1}$, a value consistent with the diffusion limited reaction. The transient absorption data indicates that oxidized halide photoproducts only result from the diffusional quenching reactions, and not from static quenching with an associated iodide ion. Fast back-electron transfer rates and low cage-escape yields in the ruthenium:iodide assemblies are invoked to explain why the static quenching pathway does not lead to measurable photoproduct yields.

Introduction

Excited-state electron transfer reactions are of significant interest in chemistry, particularly in the fields of photoredox catalysis [1] and solar energy conversion [2]. Radiative and non-radiative decay pathways are often kinetically competitive with electron transfer, especially when the free energy change is small. To enhance efficiencies and impart greater control over excited-state reactions, the tools of supramolecular assembly have been utilized to self-assemble the redox-active reactants with the photocatalyst in the ground state, thereby precluding the need for diffusion. This strategy has been implemented in asymmetric catalysis, enabling high enantioselectivity with chiral hydrogen-bonding photocatalysts [3–6], supramolecular electron-transfer reactions [7,8], and in halide oxidation with cationic photocatalysts that afford halogen atoms on the nanosecond time scale [9–11]. In many of these cases, preorganization has indeed provided access to novel mechanisms, but the formation of strong ground-state assemblies also has unintended consequences, such as reactant stabilization that inhibit desired reactivity [10]. Herein we report the structural and photophysical properties of dicationic photocatalysts with functional groups for halide coordination that self-assemble in a 1:2 photocatalyst:halide stoichiometry.

The development of new photocatalysts that promote reactant assembly and initiate excited-state electron transfer is expected to be impactful. Ruthenium polypyridyl photocatalysts are suited for such fundamental study as they possess long-lived and well-characterized metal-to-ligand charge transfer (MLCT) excited states with high stability in adjacent redox states. Of particular interest are photocatalysts that bear amide functional groups in the 4,4′ or 5,5′ positions of a 2,2′-bipyridine ligand [10,12–17] that are known to associate with halides in organic solvents. Reductive quenching of the excited state by a halide generates a halogen atom that may react with another halide to form a X-X covalent bond. Hence supramolecular assemblies that afford both excited-state electron transfer and the subsequent bond formation reactivity are of particular interest. Study of such assemblies may one day enable the selective oxidation of chloride in sea water for example.

Herein, three ruthenium polypyridyl photocatalysts shown in Fig. 1 were found to self-assemble with chloride, bromide, and iodide in CH_3CN solutions. Large equilibrium constants for association of one and two halide ions (K_{11} from $10^4 - 10^6\ M^{-1}$, K_{12} from $10^3 - 10^5\ M^{-1}$) were quantified. The ground-state assembly had a significant impact on the excited-state quenching reaction with iodide for Ru-btfmb.

* Corresponding author at: UNC-Chapel Hill: The University of North Carolina Chapel Hill, United States.
E-mail address: gjmeyer@email.unc.edu (G.J. Meyer).

https://doi.org/10.1016/j.jpap.2021.100090
Received 1 September 2021; Received in revised form 27 November 2021; Accepted 29 November 2021
Available online 2 December 2021

Results

Synthesis

The synthesis of the amide-functionalized halide receptor ligand **5,5′-daea** was achieved through the modification of a literature procedure [17]. Briefly, the methyl groups of 5,5-dimethyl-2,2′-bipyridine were oxidized to carboxylic acids by excess potassium dichromate in sulfuric acid. Esterification of the carboxylic acid groups was performed in ethanol with catalytic sulfuric acid, yielding 5,5′-diethylester-2,2′-bipyridine, which, when refluxed in the presence of 2-(2-aminoethylamine)ethanol, gave **5,5′-daea** as a white precipitate. The yields for each step of the ligand synthesis ranged from 34 to 93%.

The ruthenium complexes **Ru-dtb, Ru-bpy**, and **Ru-btfmb** shown in Fig. 1 were prepared by refluxing the appropriate $Ru(LL)_2Cl_2$ (LL = dtb, bpy, btfmb) precursor with **5,5′-daea** in ethanol. The reaction mixture was purified by column chromatography and the desired photocatalysts were precipitated as the PF_6 salt in moderate yields (32–64%). Characterization of the **5,5′-daea** ligand with ^{1}H NMR and the photocatalysts with ^{1}H NMR and high resolution mass spectroscopy, is provided in the SI (Figures S1-S7).

Electrochemistry and absorption spectroscopy

Square-wave voltammetry (Figure S8) was used to determine the metal-based $Ru^{III/II}$ and ligand based reduction potentials of each complex (Table 1). The $Ru^{III/II}$ potentials were sensitive to the electronic properties of the ancillary ligands, with electron withdrawing groups yielding the most positive $Ru^{III/II}$ potential (1.84 V vs NHE for **Ru-btfmb**), while electron donating groups gave the most negative $Ru^{III/II}$ potential (1.46 V vs NHE **Ru-dtb**). A comparison of the ligand-based reduction potentials with those of the homolyptic complexes indicated that for **Ru-btfmb**, the first reduction is of the btfmb ligand [18]. For **Ru-dtb** and **Ru-bpy**, the first reduction potential, which is approximately the same for both complexes, did not align with either dtb [19] or bpy [20], and is therefore ascribed to reduction of the 5,5′-daea ligand. Blakley and DeArmond indicated that the excited-state is localized on the most easily reduced ligand [21]. Therefore, in **Ru-btfmb** the excited-state is localized on the btfmb ligand and on the 5,5′-daea ligand for **Ru-bpy** and **Ru-dtb**.

The UV–visible absorption spectra of the photocatalysts are shown in Fig. 2. Characteristic features include the broad MLCT absorption between 400 and 550 nm and sharp absorption profiles at or below 300 nm attributed to ligand centered π-π* transitions. Visible light excitation resulted in room temperature photoluminescence.

Halide assembly

The titration of tetrabutylammonium (TBA) chloride, bromide, or iodide salts into CH_3CN (or CH_2Cl_2) solutions of the ruthenium photocatalysts (~ 40–60 μM) impacted the UV-visible absorption spectrum and provided a means to quantify halide assembly. The addition of chloride to **Ru-dtb** in CH_2Cl_2 resulted in a dramatic color change from red to orange that was visible to the naked eye (Figure S9). The same Cl^- addition in CH_3CN resulted in a smaller color change that was not discernable by eye, Fig. 3. In CH_3CN, halide addition to **Ru-dtb** (Fig. 3, left, and Figure S10) and to **Ru-bpy** (Figure S11) resulted in a blue shift of the low energy MLCT transitions, while for **Ru-btfmb** halide addition induced a red-shift (Fig. 3, right, and Figure S12). Notably, in all acetonitrile halide titrations, no isosbestic points were observed at low halide concentration and were resolved at higher halide concentrations (Fig. 3, dashed lines in insets). The spectral changes induced by the halides were fit to a 1:2 Ru:2X^- binding model to determine the equilibrium constants for halide assembly [22,23]. The equilibrium constants are given for each photocatalyst with chloride, bromide, and iodide in Table 2, which enabled the mole fractions of the Ru^{2+}, [Ru^{2+}, X^-], and [Ru^{2+},2X^-] species at each halide concentration to be determined (Figure S13).

Halide titrations into ~ 1 mM **Ru-dtb, Ru-bpy**, or **Ru-btfmb** CD_3CN solutions were monitored by ^{1}H NMR spectroscopy (Fig. 4, and Figure S14). For **Ru-dtb**, the most prominent shifts were observed for the amide H atoms and the 4,4′ hydrogens of the 5,5′-daea ligand, which shifted downfield by 1.84 and 0.57 ppm, respectively. The changes associated with the 4,4′ hydrogens saturated at ~ 2.5 equivalents of chloride, while the amide hydrogens shifted continuously throughout the course of the titration. Small downfield shifts were also observed for the 6,6′ hydrogens (Δppm = 0.16) on the 5,5′-daea ligand, and the 5,5′ hydrogens (Δppm = 0.12) on the dtb ligand. The results for **Ru-btfmb** and **Ru-bpy** were qualitatively similar for the amide, 4,4′, and 6,6′ hydrogens on 5,5′-daea, and 5,5′ on the ancillary ligand. However, for **Ru-btfmb**, the 4,4′ hydrogens on the amide-functionalized ligand underwent a much smaller (0.13 ppm) shift while the 6,6′ hydrogens on that ligand had a larger Δppm of 0.20.

Titrations in the less polar solvent CD_2Cl_2 provided additional insight into supramolecular assembly with **Ru-dtb** (Figure S15). The same amide, 4,4′ and 6,6′ hydrogens on the 5,5′-daea ligand, and 5,5′ hydrogens on the dtb ligand shifted downfield but, the 4,4′ hydrogens on the 5,5′-daea ligand displayed a much larger shift (Δppm = 0.73) with 1.5 equivalents of chloride. In addition, higher chloride concentrations resulted in an upfield shift of 0.29 ppm that was not observed in CH_3CN. Additionally, the 5,5′ hydrogens on the dtb ligand were insensitive to the Cl^- ions until concentrations greater than 1.5 mM (~1.5 eq) resulted in a 0.21 ppm shift.

Table 1
Ground- and excited-state reduction potentials of ruthenium photocatalysts.[a].

(V vs NHE)				
Complex	$Ru^{III/II}$[a]	$Ru^{2+/+}$	$Ru^{2+*/+}$	ΔG_{ES} (eV)
Ru-btfmb	1.84	−0.62	1.56	2.18
Ru-bpy	1.54	−0.72	1.31	2.03
Ru-dtb	1.46	−0.74	1.21	1.95

[a] Ground-state potentials measured in 0.1 M $NaClO_4/CH_3CN$.

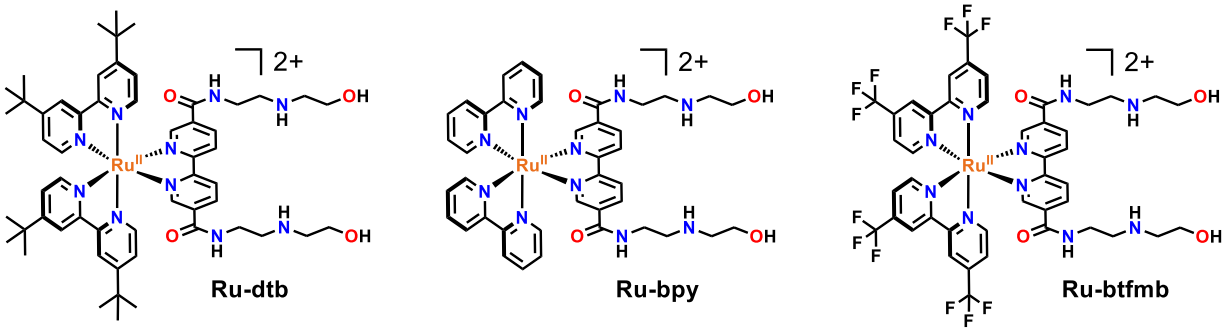

Fig. 1. Ruthenium polypyridyl photocatalysts utilized in this study for supramolecular assembly with halides.

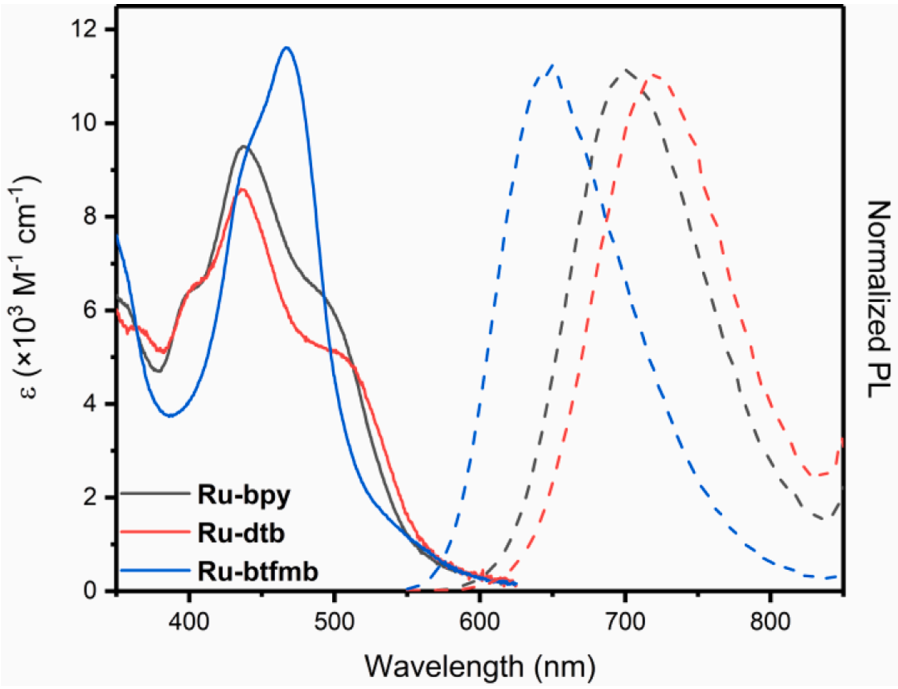

Fig. 2. Absorbance (solid lines) and photoluminescence (dashed lines) spectra of the ruthenium photocatalysts in CH_3CN.

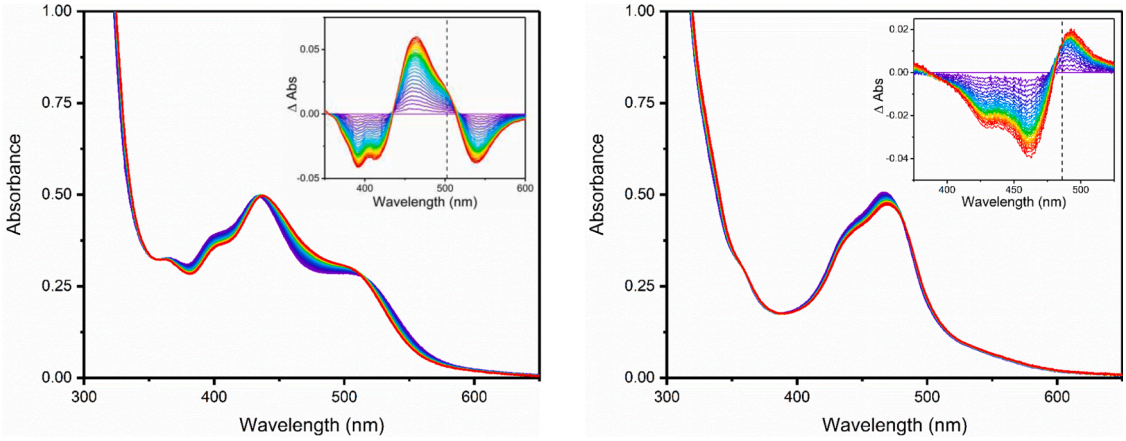

Fig. 3. Absorption spectra of Ru-dtb (left) and Ru-btfmb (right) ~50 μM in CH_3CN) with added tetrabutylammonium chloride (from 0 to ~500 μM, or 0 to 10 equivalents). The insets show ΔAbs spectra (obtained by subtracting the absorbance at each halide concentration from the spectrum without halides) that show a lack of isosbestic points at low chloride concentration and the appearance of a new isosbestic point (dashed lines) at higher concentrations.

Table 2
Equilibrium constants for halide-photocatalyst assemblies.

	M^{-1}	Ru-dtb	Ru-bpy	Ru-btfmb
Cl^-	K_{11}	$4.7 \pm 0.1 \times 10^5$	$2 \pm 1 \times 10^6$	$2 \pm 1 \times 10^6$
	K_{12}	$1.3 \pm 0.2 \times 10^3$	$2.8 \pm 0.8 \times 10^5$	$2.0 \pm 0.7 \times 10^4$
Br^-	K_{11}	$2.5 \pm 0.5 \times 10^5$	$7 \pm 3 \times 10^5$	$5 \pm 3 \times 10^5$
	K_{12}	$5 \pm 4 \times 10^3$	$3 \pm 1 \times 10^4$	$9 \pm 4 \times 10^3$
I^-	K_{11}	$4 \pm 1 \times 10^4$	$4 \pm 2 \times 10^4$	$1.1 \pm 0.1 \times 10^5$
	K_{12}	$9 \pm 2 \times 10^2$	$1 \pm 1 \times 10^3$	$1.4 \pm 0.3 \times 10^3$

Excited-state behavior with halide

Visible light excitation of **Ru-dtb, Ru-bpy**, and **Ru-btfmb** resulted in photoluminescence (PL) with maxima centered between 650 and 750 nm, Fig. 2. Time-resolved PL decays measured after pulsed-light excitation were well described by a first-order kinetic model with lifetimes that ranged from 44 ns (**Ru-dtb**) to 875 ns (**Ru-btfmb**) ns, Table 3. The PL quantum yields, as well as radiative and non-radiative rate constants are also given in Table 3 [24]. The free energy stored in the excited-state, ΔG_{ES}, was estimated by extrapolation of the high energy region of the PL spectrum to the photon energy-intercept, Table 1. With the $E^o(Ru^{2+/+})$ potential and ΔG_{ES}, the excited state reduction potential $E^o(Ru^{2+*/+})$, was determined with Eq. (1).

$$E^0\left(Ru^{2+*/+}\right) = \Delta G_{ES} + E^0\left(Ru^{2+/+}\right) \quad (1)$$

Halide addition impacted the PL spectra and lifetimes. For **Ru-dtb** and **Ru-bpy**, halides induced a blue shift and an increase in the PL intensity (Figures S16) and lifetime. However, for **Ru-btfmb**, the addition of chloride and bromide led to a red shift and a small decrease in the PL intensity (Figures S17), while iodide addition resulted in dramatic excited-state quenching, Fig. 5. Both the initial PL intensity and the lifetime of **Ru-btfmb*** decreased with increasing iodide concentration. Stern-Volmer analysis (Eq. (2)) of the static and dynamic component

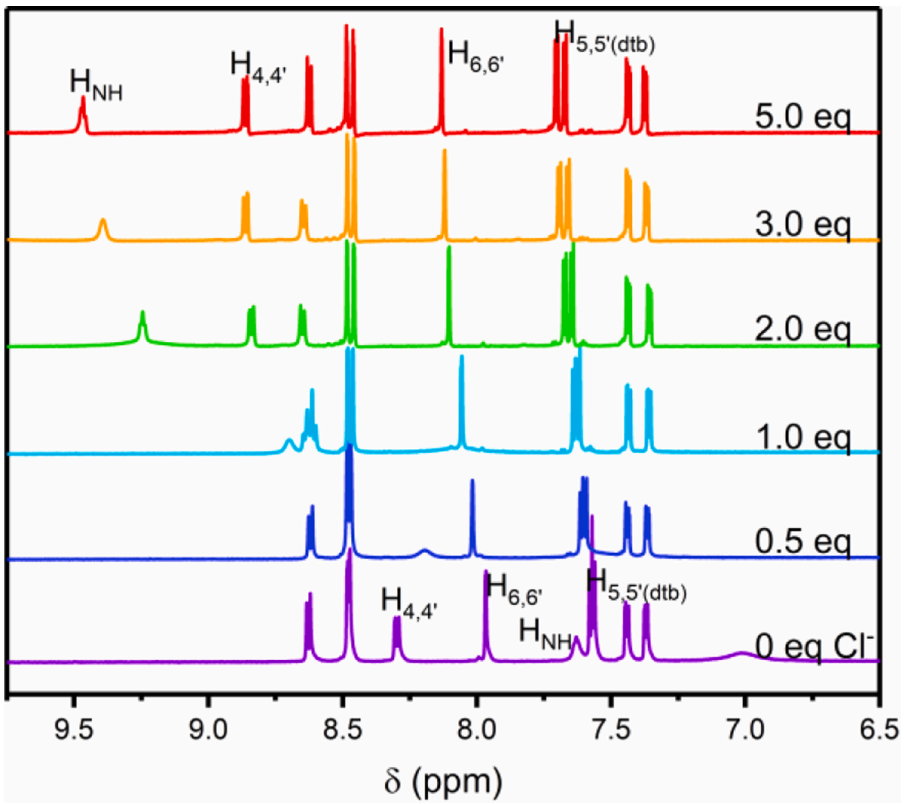

Fig. 4. The ^{1}H NMR spectra of Ru-dtb (~1 mM) with the indicated number of TBACl equivalents in CD_3CN.

Table 3
Photophysical properties of the ruthenium photocatalysts.

Complex	λ_{max} PL (nm)	τ (ns)	Φ_{PL}	k_r ($\times 10^4$ s^{-1})	k_{nr} ($\times 10^6$ s^{-1})
Ru-dtb	720	44	0.002	4.5	22.58
Ru-bpy	700	57	0.003	5.2	17.58
Ru-btfmb	645	875	0.046	5.3	1.09

yielded two linear regions, one at low (0–10 μM) and the other at high (20–100 μM) iodide concentrations, Fig. 5, right inset. The dynamic quenching rate constant, k_q, calculated with Eq. (3) was 6.8×10^{10} M^{-1} s^{-1} and 4.0×10^{10} M^{-1} s^{-1}. The static quenching constants were 2.4×10^4 M^{-1} and 1.3×10^3 M^{-1} at low and high iodide concentrations, respectively.

$$I_0/I \text{ or } \tau_0/\tau = 1 + K_{SV}[Q] \quad (2)$$

$$k_q = K_{SV}/\tau_0 \quad (3)$$

The excited-state quenching of **Ru-btfmb** was further probed at ionic strengths μ = 0.005 – 0.1 M with $TBAClO_4$ as an inert electrolyte. In these electrolyte solutions, the static quenching was drastically attenuated. Increasing the ionic strength also resulted in a decrease in the dynamic quenching rate constants (k_q) (Figure S18), allowing a Debye-

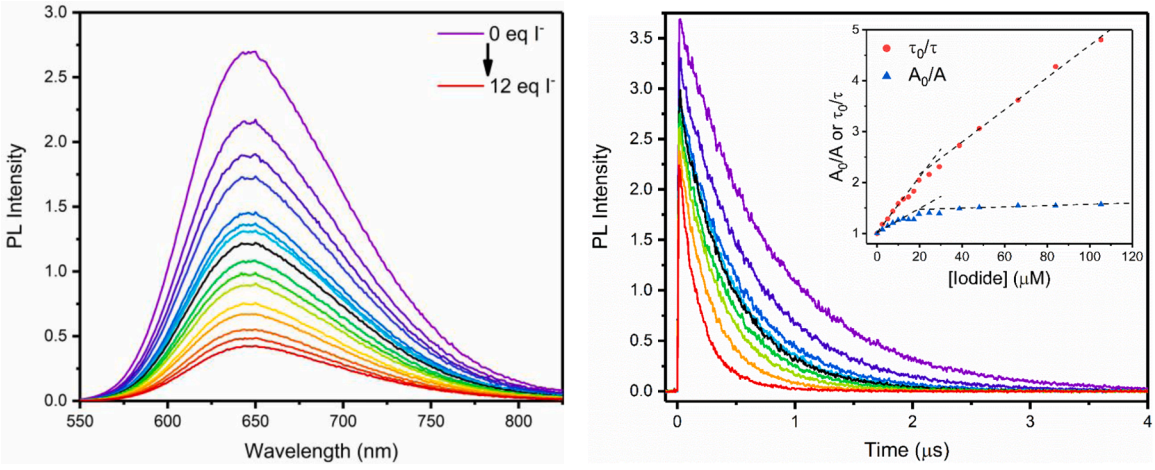

Fig. 5. Photoluminescence spectra (left) and lifetime (right) quenching of Ru-btfmb (~10 mM in CH_3CN) by iodide (0 to 100 μM, 0 to 10 equivalents). The black trace in the steady-state and time-resolved PL indicates the TBA iodide concentration (~20 mM) at which the maximum concentration of $[Ru^{2+},I^{-}]^{+}$ is formed. The inset shows a Stern-Volmer plot for the time-resolved PL, where the dynamic (τ_0/τ, red dots) and static (A_0/A, blue triangles, A = initial PL amplitude) quenching are overlaid with linear fits at low (0–10 \μM) and high (20–100 μM) iodide concentrations.

Hückel analysis to be performed, *Eq. (4)*.

$$\log(k) = \log(k_0) + \frac{2Az_a z_b \mu^{1/2}}{1 + \alpha\beta\mu^{1/2}} \quad (4)$$

A plot of $2A\mu^{1/2}/(1+\alpha\beta\mu^{1/2})$ (where A and β are constants, 1.1611 and 3.274×10^9 [25], and α, the reactive radius is 5.5 Å) versus $\log(k_q)$ is expected to result in a linear relationship where the y-intercept equals k_q at $\mu = 0$, and the slope equals the charge of the two ionic species ($z_a z_b$). For this data, a linear fit gave a k_q at $\mu = 0$ of 6.3×10^{10} M^{-1} s^{-1} and a slope of −2.

Transient absorption spectroscopy was performed on ~40 μM **Ru-btfmb** solutions in CH_3CN. The transient spectra of **Ru-btfmb** upon pulsed 532 nm excitation displayed a ground-state bleach centered at 460 nm and growths below 400 nm and above 520 nm with isosbestic points at 419 and 520 nm, Fig. 6, left. When excess iodide (~1 mM, 25 eq. with respect to **Ru-btfmb**) was present in the solution, new absorption features were observed. These features were successfully modeled (Fig. 6, middle) with the known spectrum of diiodide, $I_2^{\bullet-}$, ($\lambda_{max} = 385$ nm), the spectrum of the reduced ruthenium complex (Ru^+, $\lambda_{max} = 520$ nm, measured in Figure S19), and the ground-/ excited-state Δ absorption spectrum. At all iodide concentrations investigated, Ru^+ (monitored at 520 nm) appeared before $I_2^{\bullet-}$ (monitored at 419 nm), indicating that the oxidized halide species was a secondary photoproduct (Fig. 6, right). A titration experiment was performed to measure the second-order rate constant for Ru^+ and $I_2^{\bullet-}$ formation, which were found to be 2.5×10^{10} M^{-1} s^{-1} (Figure S20).

Discussion

Three ruthenium polypyridyl photocatalysts were shown to assemble with two halide ions in CH_3CN. Although hosts for association with multiple anions are an active area of research [26], few examples of such ruthenium complexes have been investigated, and highly charged cationic complexes and/or low dielectric solvents were required in the limited previous examples [11,27,28]. The approach described herein makes use of amide functional groups in the 5,5′ position of a bipyridine ligand to facilitate large equilibrium constants with halide in a polar solvent. This result was somewhat unexpected, as one-to-one ruthenium-to-halide assemblies were exclusively observed for related dicationic photocatlysts with amide functional groups in the 4,4′ position [10,16,17,29].

For **Ru-dtb** and **Ru-bpy**, there was no experimental evidence for light-driven halide oxidation. Instead, halide assembly increased the excited-state lifetime and resulted in a blue shift of the PL spectra. For **Ru-btfmb**, both static and dynamic quenching by iodide was observed. A Stern-Volmer analysis revealed two linear regions from which the of the static and dynamic quenching constants were extracted. Transient absorption experiments revealed that the quenching proceeds through an electron-transfer reaction with only the dynamic component yielding long-lived reduced photocatalysts and $I_2^{\bullet-}$ products. Below we discuss the supramolecular structure followed by the excited-state reaction chemistry.

Supramolecular assembly structure

Chloride titrations of **Ru-dtb** in CH_2Cl_2 solutions were particularly revealing as they provided clear evidence for both a 1:1 and a 1:2 ruthenium:chloride assembly. In the UV-visible absorption spectra, three species with distinct absorption profiles were resolved (Figure S10), while the binding isotherms provided evidence of two halide association steps to form $[Ru^{2+},Cl^-]^+$ and $[Ru^{2+},2Cl^-]$. The spectral changes associated with chloride assembly were dramatic and observable by eye, as the red solution turned yellow-orange. These visible changes suggest that the complex may be promising for applications in colorimetric halide sensing.

The ^1H NMR spectrum of **Ru-dtb** in CD_2Cl_2 provided additional evidence for the formation of 1:2 assemblies with chloride (Figure S15). In particular, the 4,4′ hydrogens on the 5,5′-daea ligand experienced a significant downfield shift (Δppm = 0.73), behavior attributed to interactions that lengthen the C—H bond and deshield the hydrogen. However, increasing the chloride concentration past 1.5 equivalents resulted in an upfield shift of 0.29 ppm for these same hydrogens, indicative of association of a second chloride that destabilizes the first and results in less productive interactions at the 4,4′ position. The total downfield shift of 0.43 ppm (0.73 downfield minus 0.29 upfield) experienced during the course of the titration indicates that the 4,4′ hydrogens contribute to beneficial interactions in the 1:2 halide assembly, but to a less extent than in the 1:1 assembly. Although CH_2Cl_2 proved to be a useful solvent for identifying the presence of both the 1:1 and 1:2 ruthenium-to-halide assemblies, a more complete characterization of halide association and excited-state quenching was performed in CH_3CN, a solvent in which all three complexes were soluble.

Significant research on anion association and sensing has shown that equilibrium constants for assembly are inversely proportional to the solvent dielectric [30], as beneficial solvation interactions with the anion compete with stabilization by the photocatalyst. As CH_3CN ($\varepsilon = 37.5$) is significantly more polar than CH_2Cl_2 ($\varepsilon = 8.93$), the equilibrium constants with halide were expected to decrease, possibly to such an extent that a second halide association would not occur. However, addition of halide salts (chloride, bromide, and iodide) to CH_3CN solutions of **Ru-dtb, Ru-bpy**, and **Ru-btfmb** resulted in several distinct spectral features that were consistent with 1:2 ruthenium-to-halide assembly. For all complexes, isosbestic points were absent at low halide concentration, behavior consistent with more than two light absorbing species [16,17]. Additionally, secondary isosbestic points were resolved at high halide concentrations, consistent with the conversion of $[Ru^{2+},X^-]^+$ to $[Ru^{2+},2X^-]$. Finally, fitting the spectral data to a 1:2 model

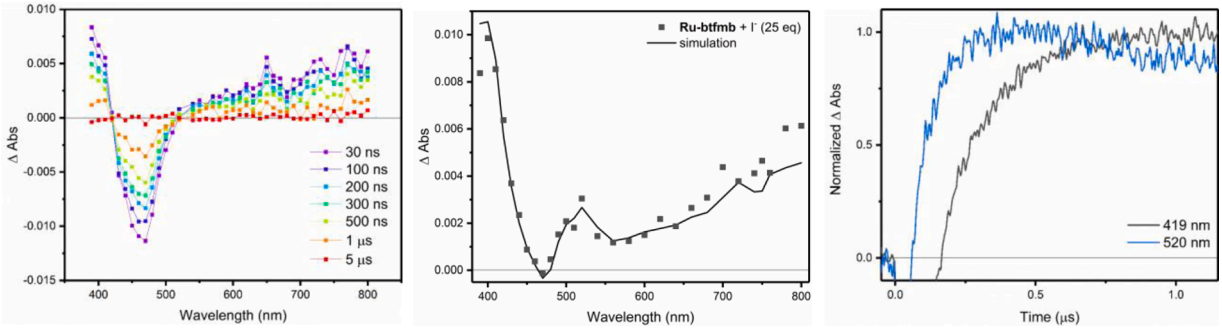

Fig. 6. Absorption difference spectra measured at the indicated delay times after pulsed 532 nm excitation of Ru-btfmb (~40 μM) in CH_3CN (left), and at 200 ns in the presence of 20 eq of iodide (middle). The absorption changes of Ru-btfmb (~40 μM) with 5 eq of iodide monitored at 419 and 520 nm (right). The laser fluence was ~5 mJ/pulse.

generated residuals that were randomly distributed about zero while residuals for the 1:1 model showed systematic deviations. Thordarson suggests that residuals provides a means to distinguish equilibrium models [22,23], suggesting that the 1:1 model should not be used in this case. Based on these observations, a 1:2 ruthenium-to-halide stoichiometry was used to describe the data in CH_3CN, and modeling the data in this way gave the equilibrium constants (K_{11} and K_{12}) for halide association shown in Table 2. From the equilibrium constants, the mole fractions (χ) of the ruthenium species, Ru^{2+}, $[Ru^{2+},X^-]^+$, and $[Ru^{2+},2X^-]$, at each point during the titration were determined. The $[Ru^{2+},X^-]^+$ species was dominate after one equivalent of halide was added. For chloride and bromide, K_{12} was so large that when ~10 eq of X^- was titrated, the major (70–80%) species was the 1:2 $[Ru^{2+},2X^-]$ assembly.

A brief inspection of the equilibrium constants reveals that the complexes are most selective for chloride association, with large K_{11} (0.5 to 2 × 10^6 M^{-1} s^{-1}) and K_{12} (0.01 to 3 × 10^5 M^{-1} s^{-1}) values. As the charge-to-size ratio of the halide decreases, K_{11} decreased anywhere from a factor of two to ten going from chloride to bromide, and again from bromide to iodide. Comparing the equilibrium constants for each complex in the presence of the same halide provided some insight into the supramolecular assembly structure. For example, **Ru-dtb, Ru-bpy**, and **Ru-btfmb** association with chloride gave values of K_{11} that were within a factor of four, while association with bromide and iodide gave K_{11} values that varied by a factor of two or less. As the ancillary ligands do not dramatically impact K_{11}, the first association is likely occurring with the 5,5′-daea ligand. Inspection of the K_{12} values for chloride association revealed that the second stepwise equilibria varied much more significantly with the identity of the ancillary ligand. For association of the second halide, increasing the steric bulk of the functional group at the 4,4′ position resulted in nearly an order of magnitude decrease going from H to CF_3, and again from CF_3 to *t*-butyl. This suggests that the second halide interacts, at least in part, with the ancillary ligand, and that bulky substituents inhibit this interaction. For iodide and bromide however, the sterics of the ancillary ligands appears less influential, as K_{12} was approximately the same for all three photocatlysts. This suggests that the size of the larger halides already inhibits the approach to the second receptor site.

Additional insight into the assembly structures was gained through ^1H NMR spectroscopy in CD_3CN. The most significant shifts were observed for the amide H atoms and 4,4′ hydrogens on the 5,5′-daea ligand. The downfield shifts of the 4,4′ hydrogens on the daea ligand saturate before the amide hydrogens and other resonances that shift in the presence of chloride, suggesting that the first halide assembles predominately with the 4,4′ and amide hydrogens on the 5,5′-daea ligand, Scheme 1 left hand side. At higher halide concentrations, downfield shifts were observed for the 6,6′ hydrogens on the 5,5′-daea ligand, and for the 5,5′ hydrogens on the ancillary ligands. Therefore, the second halide likely assembles between the amide functionalized and ancillary ligand, close to the ruthenium metal center, Scheme 1, right hand side. Free rotation of the second amide group allows additional halide stabilization of this halide in agreement with the amide hydrogens continual downfield shift. Although these proposed structures break the symmetry of the complex and the 5,5′-daea ligand, fast exchange on the NMR timescale is expected and likely leads to averaging of the hydrogens in different environments.

Excited-state reaction chemistry

Light-excitation into the MLCT absorbance of **Ru-dtb, Ru-bpy**, and **Ru-btfmb** resulted in room temperature photoluminescence, PL. For **Ru-dtb** and **Ru-bpy**, the excited-state had an electron localized on the 5,5′-daea ligand, while for **Ru-btfmb**, the electron was localized on the ancillary btfmb ligand. The assembly of halide anions was found to perturb the luminescent excited-state in a manner that was dependent on the interaction of the halide with the excited-state dipole. For example, halide addition to **Ru-dtb** and **Ru-bpy** resulted in a blue-shift and increase in the PL intensity. This behavior was ascribed to a coulombic repulsion between the excited-state dipole and the assembled halide, resulting in a destabilization of the excited state. For **Ru-btfmb**, where the excited-state dipole increases the coulombic attraction with the assembled halide (X^- = chloride and bromide), a redshift and decrease in the photoluminescence intensity was observed, as is expected from a stabilization of the excited state.

The excited-state behavior of **Ru-btfmb** in the presence of iodide could not be explained solely by the excited-state dipole orientation as significant quenching was observed. The excited state reduction potential ($Ru^{2+*/+}$) of **Ru-btfmb** reveals it to be a potent photooxidant ($Ru^{2+*/+}$ = 1.56 V vs NHE) capable of iodide oxidation ($I^{\bullet/-}$ = 1.23 V vs NHE). In contrast, significantly less driving force for iodide oxidation exists for **Ru-dtb*** and **Ru-bpy***. A Stern-Volmer analysis of the time-resolved quenching of **Ru-btfmb*** by iodide showed two regimes where the expected linear relationship between the excited-state lifetime (τ_0/τ, dynamic) or the initial PL intensity (A_0/A, static) and the iodide concentration was evident. To describe the unusual Stern-Volmer behavior, it is helpful to consider the possible quenching mechanisms of the ruthenium:iodide assemblies present in solution, depicted in Scheme 2.

As determined from the characterization of the ground state halide assembly, **Ru-btfmb** can be present in CH_3CN solution with zero, one, or two assembled iodide anions. At low iodide concentrations (<1 eq. with regard to ruthenium), Ru^{2+} is the predominate species in solution (Figure S13, right). However, after this point, the equilibrium favors formation of $[Ru^{2+},I^-]^+$, and the Ru^{2+} concentration approaches zero. At ~2.5 eq. of iodide, the concentration of $[Ru^{2+},I^-]^+$ reaches its maximum value, after which its gradual decrease is concomitant with an increase in the $[Ru^{2+},2I^-]$ concentration. Quenching of the luminescent excited state reaches 85% by ~12 eq. of iodide, which is well before $[Ru^{2+},2I^-]$ becomes the dominate species in solution. Under the conditions described above, Ru^{2+} and $[Ru^{2+},I^-]^+$ are present in concentrations where dynamic quenching would be observed, while static

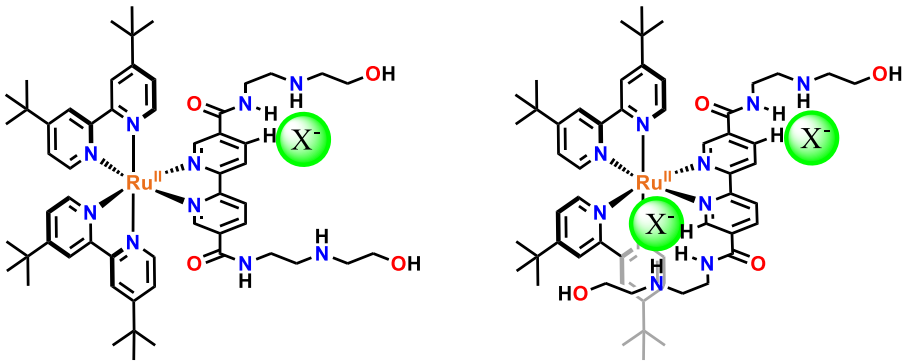

Scheme 1. Proposed structure of the $[Ru^{2+},X^-]^+$ (left) and $[Ru^{2+},2X^-]$ (right) assemblies.

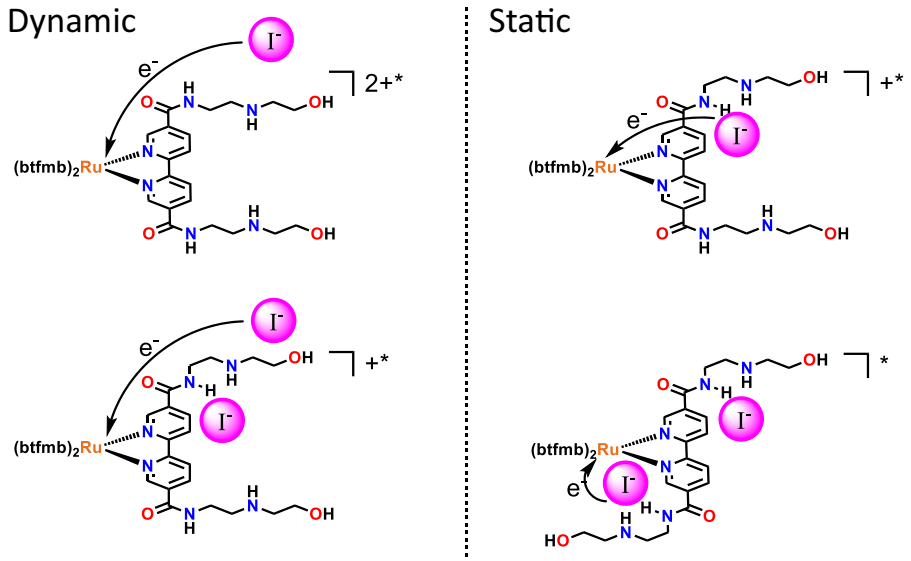

Scheme 2. Proposed dynamic and static quenching mechanisms of Ru-btfmb by iodide.

quenching of the assemblies $[Ru^{2+},I^-]^+$ and $[Ru^{2+},2I^-]$ would also be expected.

In the Stern-Volmer analysis of the dynamic quenching (Fig. 5, red circles), two distinct slopes are observed at low (0–10 μM, 0–1 eq.) and high (20–100 μM, 2–12 eq.) iodide concentrations, with k_q values of $6.8 \times 10^{10}\ M^{-1}\ s^{-1}$ and $4.0 \times 10^{10}\ M^{-1}\ s^{-1}$, respectively. To probe the origin of these two slopes, the excited-state quenching was performed in the presence of an inert electrolyte (TBA perchlorate) at several fixed ionic strengths ($\mu = 0.005 - 0.1$ M). Increasing the concentration of the inert electrolyte resulted in a drastic decrease in both the magnitude of static quenching and in the quenching rate constant (k_q). As relatively dilute concentrations (≤ 0.1 M) of the inert electrolyte suppressed the formation of $[Ru^{2+},I^-]^+$, the conditions required for use of Debye-Hückel theory were fulfilled, allowing the dynamic quenching of the Ru^{2+} excited-state to be solely monitored through this analysis (Figure S18). In the Debye-Hückel analysis, the slope of the linear fit yields $z_a z_b$, i.e. the product of the ionic charge, which was found to be −2, consistent with excited-state quenching of Ru^{2+} by I^-. Additionally, extrapolation of the fit to the y-axis ($\mu = 0$), where the ionic strength is equal to zero, yields the quenching rate constant for the reaction when no inert salt is present. Extrapolation to $\mu = 0$ gave a k_q of $6.3 \times 10^{10}\ M^{-1}\ s^{-1}$, which is in good agreement with the slope obtained at low iodide concentrations in the Stern-Volmer analysis. These values are also in agreement with the calculated diffusion-limited rate constant of $7.2 \times 10^{10}\ M^{-1}\ s^{-1}$ for a 2+ ruthenium polypyridyl complex and iodide, as calculated in the experimental section [31]. Therefore, at low iodide concentrations, the dynamic quenching mechanism is attributed to diffusional quenching of Ru^{2+} by iodide (Scheme 2, top left), as this is consistent with both Ru^{2+} as the main species in solution and the k_q and ionic charge obtained from the Debye-Hückel analysis.

At high iodide concentrations (20–100 μM) where $[Ru^{2+},I^-]^+$ accounts for the majority of ruthenium species, the slope from the dynamic Stern-Volmer quenching was found to be $4.0 \times 10^{10}\ M^{-1}\ s^{-1}$. In this instance, the Debye- Hückel analysis could not be used to probe diffusional quenching of $[Ru^{2+},I^-]^+$, as the presence of the inert electrolyte attenuates supramolecular assembly to such an extent that it is not significantly observed. Instead, the diffusion-limited rate constant for the monocationic assembly $[Ru^{2+},I^-]^+$ and iodide were calculated. When all other variables were held constant, decreasing the charge of the ruthenium species by one (through assembly with an iodide anion) will slow diffusion to $4.7 \times 10^{10}\ M^{-1}\ s^{-1}$, which is in excellent agreement with the value obtained from the Stern-Volmer plot at high iodide concentrations. This suggests that diffusion-limited excited-state quenching of $[Ru^{2+},I^-]^+$ by free iodide is responsible for the second slope observed in the dynamic quenching (Scheme 2, bottom left).

Static quenching of the ruthenium excited state was also observed in titration experiments with iodide, as the initial time-resolved PL amplitude decreased with increasing iodide concentration (Fig. 5, blue triangles). The Stern-Volmer analysis of the static quenching also resulted in two sloped regions, with a K_S at low iodide concentrations (0–10 μM) of $2.4 \times 10^4\ M^{-1}$, and a K_S at high iodide concentrations (20–100 μM) of $1.3 \times 10^3\ M^{-1}$. These values are similar to the ground-state equilibrium constants obtained for the complexes through absorption spectroscopy ($K_{11} = 1.1 \times 10^5\ M^{-1}$, $K_{12} = 1.4 \times 10^3\ M^{-1}$). Additionally, at low iodide concentrations, significant concentrations of the ground-state adduct $[Ru^{2+},I^-]^+$ are found in solution with a maximum concentration of ~80% of all ruthenium species at 20 μM. At 2.5 equivalents of iodide (~25 μM) the $[Ru^{2+},I^-]^+$ concentration gradually decreases with a concurrent increase in the $[Ru^{2+},2I^-]$ concentration. Based on the values of K_S and the percentage of ruthenium species present as the $[Ru^{2+},I^-]^+$ and $[Ru^{2+},2I^-]$ adducts, the static quenching is consistent with electron transfer from an associated halide within the 1:1 (Scheme 2, top right) or 1:2 (Scheme 2, bottom right) ion-pair at low and high iodide concentrations, respectively.

The ground-state equilibrium constants and excited-state quenching data implies that the ruthenium photocatalyst **Ru-btfmb** is capable of promoting halide oxidation reactions within the 1:1 and 1:2 ruthenium: iodide assemblies. This reaction is of particular interest in solar energy conversion, as photogenerated $I^\bullet$ atoms are known to react with I^- to form $I_2^{\bullet-}$, thereby storing energy in chemical bonds. The **Ru-btfmb** photocatalyst was designed to bring two associated I^- atoms in close proximity with the goal of prearranging the reactants and thereby precluding diffusion. To investigate the efficiency of this strategy, the products of the excited-state quenching reaction were monitored with time-resolved transient absorption spectroscopy. The absorption profile of excited-state **Ru-btfmb** is typical of ruthenium polypyridyl complexes (Fiugre 6, left) with growths below 400 nm and above 520 nm, a ground-state bleach centered at 460 nm, and ground/excited-state isosbestic points at 419 and 520 nm. In the presence of excess iodide (~25 eq.) new spectral features are observed with maximum at 400 and 520 nm (Fig. 6, middle). These features are consistent with the known spectra of $I_2^{\bullet-}$ ($\lambda_{max} = 385$ nm) and the reduced ruthenium complex (Figure S19) and the transient spectrum was indeed well-modeled as a sum of Ru^{2+*}, Ru^+, and $I_2^{\bullet-}$ spectra. To probe the kinetics of photoproduct formation, the rate of Ru^+ and $I_2^{\bullet-}$ formation was monitored as a function of the iodide concentration. Visual inspection of the kinetic traces shows that the rate

of $I_2^{\bullet-}$ formation at each iodide concentration is slower than the rate of formation of Ru^+, suggesting that $I_2^{\bullet-}$ is a secondary photoproduct. The formation of $I_2^{\bullet-}$ was also shown to be dependent on the free iodide concentration with a second order rate constant of 2.5×10^{10} M^{-1} s^{-1}. This value is in good agreement with the known diffusion limited rate constant for the $I^{\bullet} + I^-$ reaction to yield $I_2^{\bullet-}$.[31] The transient data suggests that the mechanism for photoproduct generation is that depicted in Eqs. (5)–6, where first a ruthenium excited-state is diffusionally quenched by iodide to generate Ru^+ and $I^{\bullet}$, and then the $I^{\bullet}$ atom reacts with a solvated I^- to form $I_2^{\bullet-}$.

$$Ru^{2+*} + I^- \rightarrow Ru^+ + I^{\bullet} \quad (5)$$

$$I^{\bullet} + I^- \rightarrow I_2^{\bullet-} \quad (6)$$

From the transient absorption data, no evidence was obtained for an iodide oxidation mechanism in which the electron transfer and bond formation occurred within the $[Ru^{2+},2I^-]$ assembly, as might have been expected. In fact, even static quenching of the ruthenium excited-state was not observed with this method. To explain this, we suggest that when electron transfer occurs within the excited-state assembly, diffusion of the iodine atom is precluded by fast back-electron transfer. Fast back-electron transfer and a low cage escape yield would result in small amounts of product formed by this pathway, which would render detection difficult within the time-resolution of our instrument. In the diffusional reaction, cage escape yield of the oxidized halide is expected to be larger, which is in agreement with the data presented above.

Conclusion

A series of ruthenium polypyridyl complexes with amide functionalized bipyridine ligands and electron donating or withdrawing ancillary ligands were studied for halide assembly and oxidation. In CH_3CN (and when soluble, CH_2Cl_2), spectral evidence was obtained for 1:2 ruthenium:halide assemblies, and large equilibrium constants for association of the first (K_{11} from 10^4 to 10^6 M^{-1}) and second halide (K_{12} from 10^3 to 10^5 M^{-1}) were measured. The electronic properties of the ancillary ligands tuned the excited-state reduction potential ($Ru^{2+*/+}$) by 350 meV. For the most potent photo-oxidant, static and dynamic quenching of the luminescent excited state by iodide was resolved. A Stern-Volmer analysis of both the static and dynamic components revealed two regions at low and high iodide concentrations, consistent with diffusion limited quenching of Ru^{2+} and $[Ru^{2+},I^-]^+$, and static quenching of $[Ru^{2+},I^-]^+$ and $[Ru^{2+},2I^-]$. Transient absorption experiments were consistent with reductive quenching of the excited state to form Ru^+ and $I^{\bullet}$, while $I^{\bullet}$ subsequently reacted with free iodide, yielding $I_2^{\bullet-}$. Monitoring the kinetics of Ru^+ and $I_2^{\bullet-}$ formation suggested that only photoproducts from the diffusional reaction were able to escape the solvent cage, while fast back-electron transfer hindered mechanistic characterization of the electron transfer reaction within the assembly.

Experimental

Materials

Sulfuric acid (H_2SO_4, Fisher, 98%, Certified ACS Plus), methanol (Fisher, Certified ACS), ethanol (Fisher, Certified ACS), 2-(2-aminoethylamine)ethanol (Sigma-Aldrich, ≥ 98%), acetone (Sigma-Aldrich, Certified ACS), acetonitrile (CH_3CN, Burdick and Jackson, 99.98%), and dichloromethane (CH_2Cl_2, Burdick and Jackson, 99.98%) were used as received. Argon gas (Airgas, 99.998%) was passed through a Drierite drying tube before use. Ammonium hexafluorophosphate (NH_4PF_6, Sigma-Aldrich, ≥ 98%), tetrabutylammonium chloride (TBACl, Sigma-Aldrich, purum ≥ 97%), tetrabutylammonium bromide (TBABr, Acros Organics, 99+%), tetrabutylammonium iodide (TBAI, Sigma-Aldrich ≥ 99%), tetrabutylammonium perchlorate ($TBAClO_4$, Sigma-Aldrich, for electrochemical analysis, ≥ 99%), and ruthenium trichloride hydrate (Oakwood Chemicals, 97%) were used as received. NMR solvents were purchased from Cambridge Isotope Laboratories, Inc. 5,5′-dicarboxylic acid-(2,2′)-bipyridine [32], 5,5′-diethylester-(2,2′)-bipyridine [33], $Ru(dtb)_2Cl_2$ [34], $Ru(bpy)_2Cl_2$ [35], and $Ru(btfmb)_2Cl_2$ [36] were synthesized according to previous procedures. All solutions were sparged with argon for at least 30 min before titration, photoluminescence, and transient absorption experiments were performed.

Synthesis of the 5,5′-daea ligand

To a 100 mL round bottom flask was added 5,5′-diethylester-(2,2′)-bipyridine (1.0 g, 3.3 mmol), methanol (25 mL), and excess 2-(2-aminoethylamine)ethanol (~5 mL, ~50 mmol). The mixture was sparged with argon for ~30 min and refluxed overnight. Upon cooling, the mixture was poured into acetone (60–70 mL) causing a precipitate to form, and the solid was collected by vacuum filtration on a sintered glass frit. The precipitate was washed with excess acetone and dried under vacuum at 100 °C, yielding 5,5′-daea (0.466 g, 34%) as a white powder. ^{1}H NMR (d_6-DMSO, 400 MHz): 9.12 (2H, dd), 8.76 (2H, t,), 8.51 (2H, dd), 8.37 (2H, dd), 4.50 (2H, t), 3.45 (4H, q), 3.42 – 3.36 (4H, m), 2.72 (4H, t), 2.61 (4H, t).

Synthesis of ruthenium complexes

General method for synthesis of ruthenium complexes **Ru-dtb, Ru-bpy**, and **Ru-btfmb**. To a 50 mL round bottom flask was added the appropriate ruthenium precursor ($Ru(dtb)_2Cl_2$, $Ru(bpy)_2Cl_2$,) one equivalent of 5,5′-daea, and EtOH. The mixture was sparged with argon for ~30 min and refluxed overnight. (For **Ru-btfmb**, one equivalent of ruthenium precursor and the ligand, two equivalents of silver nitrate, and 5 mL of EtOH, were heated at 150 °C for 10 min under microwave irradiation. After this point, the procedure is the same for all three complexes.) After cooling, the red solution was filtered, and the solvent was removed by rotary evaporation. The resulting solid was dissolved in minimal MeOH and eluted through a LH-20 sephadex column with MeOH. The red band was collected, and the solvent was removed by rotary evaporation. The solid was dissolved in minimal H_2O, and a few drops of saturated aqueous NH_4PF_6 was added, causing a precipitate to form. The solid was collected with vacuum filtration, washed with excess H_2O, and dried under vacuum at 100 °C overnight, yielding a red solid.

[Ru(dtb)$_2$(5,5′-daea)](PF$_6$)$_2$, (Ru-dtb)

$Ru(dtb)_2Cl_2$ (177 mg, 0.22 mmol), 5,5′-daea (90 mg, 0.22 mmol) and ~20 mL EtOH was refluxed overnight, yielding 96 mg (33%) of **Ru-dtb**. ^{1}H NMR (CD_3CN, 400 MHz): 8.60 (2H, d), 8.48 (4H, dd), 8.33 (2H, d), 7.99 (2H, s), 7.58 (6H, m), 7.45 (2H, dd), 7.38 (2H, dd), 3.64 (4H, t), 3.48 (4H, m), 3.05 (4H, t), 2.97 (4H, t), 1.41 (36H, d). HRMS (ESI-MS). Calcd for $C_{56}H_{76}N_{10}O_4Ru$ ($[M]^{2+}$): $m/z = 527.18$ Found: $m/z = 527.25$.

Note: After the sephadex column, a luminescent impurity was still observed in the PL spectrum of **Ru-dtb**. To remove this impurity, the solid was dissolved in an CH_3CN: H_2O mixture (2% H_2O containing 1% $NaNO_3$ by mass) and eluted through a basic alumina column. A yellow band quickly eluted and was discarded, while a second red band was collected at higher percentages of H_2O (8–10%). The solvent was removed from the second fraction, yielding a red solid which was dissolved in minimal water. The addition of and a few drops of saturated aqueous NH_4PF_6 caused a precipitate to form. The solid was collected with vacuum filtration, washed with excess H_2O, and dried under vacuum at 100 °C overnight, yielding a red solid.

[Ru(bpy)$_2$(5,5′-daea)](PF$_6$)$_2$, (Ru-bpy)

$Ru(bpy)_2Cl_2$ (100 mg, 0.21 mmol), 5,5′-daea (86 mg, 0.21 mmol), silver nitrate (70 mg, 4.1 mmol) and 10 mL EtOH was refluxed

overnight, yielding 75 mg (32%) of **Ru-bpy**. ^{1}H NMR (CD_3CN, 500 MHz): 8.65 (2H, d), 8.51 (4H, d), 8.33 (2H, d), 8.08 (4H, t), 8.01 (2H, s) 7.72 (4H, t), 7.65 (2H, m), 7.41 (4H, dt), 3.70 (4H, t), 3.54 (4H, m), 3.18 (4H, t), 3.10 (4H, t). HRMS (ESI-MS). Calcd for $C_{40}H_{44}N_{10}O_4Ru$ ($[M]^{2+}$): $m/z = 415.13$ $m/z = 415.13$.

[Ru(btfmb)$_2$(5,5′-daea)](PF$_6$)$_2$, (Ru-btfmb)

$Ru(btfmb)_2Cl_2$ (100 mg, 0.13 mmol), 5,5-daea (55 mg, 0.13 mmol), silver nitrate (45 mg, 2.6 mmol) and ~5 mL EtOH was heated at 150 °C for 10 min under microwave irradiation, yielding 118 mg (64%) of **Ru-btfmb**. ^{1}H NMR (CD_3CN, 500 MHz): 8.96 (4H, d), 8.70 (2H, d), 8.43 (2H, d), 8.00 (4H, dd), 7.93 (2H, s), 7.72 (6H, m), 3.70 (4H, t), 3.54 (4H, m), 3.17 (4H, t), 3.10 (4H, t). HRMS (ESI-MS). Calcd for $C_{40}H_{44}F_{12}N_{10}O_4Ru$ ($[M]^{2+}$): $m/z = 551.11$ $m/z = 551.10$.

Nuclear magnetic resonance

Characteristic NMR spectra were obtained at room temperature on a Bruker Avance III 400 or 500 MHz spectrometer. Solvent residual peaks were used as internal standards for ^{1}H (δ =2.50 ppm for DMSO, 5.32 for CD_2Cl_2, 1.94 for CD_3CN) and ^{13}C (39.52 ppm for DMSO) chemical shift referencing. NMR spectra were processed using MNOVA.

Mass spectrometry

Samples were analyzed with a Q Exactive HF-X (ThermoFisher, Bremen, Germany) mass spectrometer. Samples were introduced via a heated electrospray source (HESI) at a flow rate of 10 μL/min. One hundred time domain transients were averaged in the mass spectrum. HESI source conditions were set as: nebulizer temperature 100 deg C, sheath gas (nitrogen) 15 arb, auxillary gas (nitrogen) 5 arb, sweep gas (nitrogen) 0 arb, capillary temperature 250 °C, RF voltage 100 V. The mass range was set to 600–2000 *m/z*. All measurements were recorded at a resolution setting of 120,000. Solutions were analyzed at 0.1 mg/mL or less based on responsiveness to the ESI mechanism. Xcalibur (ThermoFisher, Breman, Germany) was used to analyze the data. Molecular formula assignments were determined with Molecular Formula Calculator (v 1.2.3). All observed species were singly charged, as verified by unit *m/z* separation between mass spectral peaks corresponding to the ^{12}C and $^{13}C^{12}C_{c-1}$ isotope for each elemental composition.

UV−Vis absorption

UV−vis absorption spectra were recorded on a Varian Cary 60 UV−vis spectrophotometer with a resolution of 1 nm.

Steady-state PL

Steady-state PL spectra were recorded on a Horiba Fluorolog 3 fluorimeter and corrected by calibration with a standard tungsten-halogen lamp. Samples were excited at 450 nm. The intensity was integrated for 0.1 s at 1 nm resolution and averaged over 3 scans. The PL quantum yields were measured by the optically dilute method using $[Ru(bpy)_3]Cl_2$ in acetonitrile (Φ = 0.062) as a quantum yield standard [24].

Time-resolved photoluminescence

Time-resolved PL data were acquired on a nitrogen dye laser with excitation centered at 445 nm. Pulsed light excitation was achieved with a Photon Technology International (PTI) GL-301 dye laser that was pumped by a PTI GL-3300 nitrogen laser. The PL was detected by a Hamamatsu R928 PMT optically coupled to a ScienceTech Model 9010 monochromator terminated into a LeCroy Waverunner LT322 oscilloscope. Decays were monitored at the PL maximum and averaged over 180 scans. Nonradiative and radiative rate constants were calculated from the quantum yields, $\Phi = k_r/(k_r + k_{nr})$ and lifetimes, $\tau = 1/(k_r + k_{nr})$.

Electrochemistry

Square wave voltammetry was performed with a BASi Epsilon potentiostat in a standard three-cell in CH_2Cl_2 electrolytes. The cells consisted of a platinum working electrode and a platinum mesh as an auxiliary electrode. A non-aqueous silver/silver chloride electrode (Pine) was used as a reference electrode that was referenced to an internal ferrocene (630 mV vs. NHE) standard.

Halide titrations

UV−vis, PL, and time-resolved measurements were performed in CH_2Cl_2 or CH_3CN using ~10–50 μM solutions of the ruthenium complexes. Titration measurements were performed for each of the spectroscopies with TBACl, TBABr, or TBAI through additions of 0.25 equivalents. Throughout all titrations, the concentration of complexes remained unchanged. For the UV–vis titrations used to determine equilibrium constants, a stock solution of each complex was prepared with an absorbance of ~0.5 at the λ_{max}, and 5 mL was added to a quartz cuvette. A titration solution was then prepared with 10 mL of the stock solution. TBACl, TBABr, and TBAI were added to the stock solution such that a 10 μL addition to the cuvette was ~0.1 eq of halide with respect to ruthenium.

For the PL titrations, the same procedure was used, except that an absorbance of ~0.1 at the λ_{max} was used, and the concentration of halide was adjusted such that a 10 μL addition to the cuvette was ~0.25 eq of halide with respect to ruthenium. For titrations performed at a fixed ionic strength, the stock ruthenium solution was prepared in CH_3CN solution with a fixed concentration of TBA perchlorate ranging from μ = 0.005 – 0.1 M.

The ^{1}H NMR titrations were performed using a Bruker Avance III 500 MHz spectrometer equipped with a broadband inverse (BBI) probe using 1 mM ruthenium complex in 600 μL of deuterated solvent and 0.25 equivalent additions of TBACl or TBAI were added in 10 μL additions. The ruthenium concentration was kept unchanged through preparation of a titration solution that contained both the ruthenium complex and the desired halide. Each spectrum was averaged over 16 scans.

Data analysis for all experiments was performed using Origin 2017. Data fitting was preformed using a Levenberg-Marquardt iteration method. Benesi-Hildebrand type analysis was performed in Mathematica, version 11.

Diffusion calculations

The diffusional rate constants were calculated through Eq. (7) where N_A is Avogadro's number, D are the diffusion coefficients for the designated species, and β is the effective reaction radius that accounts for the attraction of the charged species, which has been previously described.

$$k_{diff} = 4\pi N_A (D_{I^-} + D_{Ru^{2+}})\beta \quad (7)$$

$$D_i = \frac{k_B T}{6\pi r_i \eta} \quad (8)$$

Diffusion coefficients were determined through the Stokes-Einstein relationship (Eq. (8)), where k_B is the Boltzmann constant, T is temperature (298 K), η is the viscosity of acetonitrile (0.369×10^{-3} Pa s), and r_i are the reactant radii where I^- = 2.06 Å and [Ru]2+ = 7.0 Å. The effective reaction radius was calculated for an ionic strength of $\mu = 4 \times 10^{-4}$ M and acetonitrile dielectric constant of $\varepsilon_r = 36.64$. The bimolecular diffusional rate constant for $[Ru]^{2+}$ and I^- was determined to be 7.22×10^{10} M^{-1} s^{-1}. The bimolecular diffusional rate constant for $\{Ru,I\}^+$ and I^- was determined to be 4.71×10^{10} M^{-1} s^{-1} [37].

Transient absorption

Nanosecond transient absorption measurements were acquired on a setup published previously [38]. Briefly, a Q-switched, pulsed Nd:YAG laser (Quantel USA (BigSky) Brilliant B 5−6 ns full width at half-maximum (fwhm), 1 Hz, ~ 10 mm in diameter) doubled to 532 nm. The laser irradiance at the sample was attenuated to 3 mJ/pulse. The probe lamp consisted of a 150 W xenon arc lamp and was pulsed at 1 Hz with 70 V during the experiment. Signal detection was achieved using a monochromator (SPEX 1702/ 04) optically coupled to an R928 photomultiplier tube (Hamamatsu) at a right angle to the excitation laser. Transient data were acquired with a computer-interfaced digital oscilloscope (LeCroy 9450, Dual 330 MHz) with an overall instrument response time of ~10 ns. An average of 30 laser pulses was acquired averaged at each wavelength of interest over the 370−800 nm range. Intervals of 10 nm were used for wavelength between 370 and 600 nm and intervals of 20 nm were used between 600 and 800 nm. Time-resolved PL data were also acquired at the same laser intensity at 532 nm.

Determination of the reduced complex extinction coefficient

The absorption spectrum of the singly reduced complex Ru^{+} was determined using a procedure adapted from literature [39]. A 10 μM solution of **Ru-btfmb** with 10 mM tri-p-tolylamine (TPA) was irradiated with 532 nm light (1.5 mJ/cm^2). Laser excitation of **Ru-btfmb** resulted in electron transfer from the TPA to Ru^{2+*}. Transient absorption spectra were recorded, normalized at 680 nm, and the normalized spectrum of the oxidized TPA was subtracted from it to give the difference spectrum between the reduced Ru^{+} and the ground state. The concentration of reduced complex formed was calculated as the extinction coefficient of the oxidized TPA is known [38]. Division of the difference spectrum by the concentration of reduced complex gave the delta extinction coefficient. Linear addition of this delta extinction coefficient to the ground-state Ru^{2+} extinction coefficient yielded the reduced complex extinction coefficient, Figure S19.

Spectral modeling

Transient absorption spectra of **Ru-btfmb** in the presence of 25 equivalents of iodide resulted in the formation of the reduced complex and diiodide. At any given time, the spectra consisted of the ground-state loss, excited states, the reduced compound, and diiodide. The kinetics monitored in the 390–800 nm wavelength range were modeled through the use of the ground state (Ru^{2+}) and reduced complex (Ru^{+}) extinction coefficients, the absorbance difference between the excited state and ground state, and the $I_2^{\bullet-}$ extinction coefficients.

Declaration of Competing Interest

The authors declare that they have no known competing financial interests or personal relationships that could have appeared to influence the work reported in this paper.

Acknowledgements

This research is supported by the National Science Foundation (NSF) under Award Number 1800022. M.D.T. would like to acknowledge the NSF Graduate Research Fellowship Program under Grant No. DGE-1650116 for support.

Supplementary materials

Supplementary material associated with this article can be found, in the online version, at doi:10.1016/j.jpap.2021.100090.

References

[1] C.K. Prier, D.A. Rankic, D.W.C. Macmillan, Chem. Rev. 113 (2013) 5322–5363.
[2] R.L. House, N.M.I. Yukie, R.L. Coppo, L. Alibabaei, B.D. Sherman, P. Kang, M. K. Brennaman, P.G. Hoertz, T.J. Meyer, J. Photochem. Photobiol. C 25 (2015) 32–45.
[3] T. Rigotti, J. Aleman, Chem. Commun. 56 (2020) 11169–11190.
[4] A. Fanourakis, P.J. Docherty, P. Chuentragool, R.J. Phipps, ACS Catal. 10 (2020) 10672–10714.
[5] R.S.J. Proctor, A.C. Colgan, R.J. Phipps, Nat. Chem. 12 (2020) 990–1004.
[6] J. Zheng, W.B. Swords, H. Jung, K.L. Skubi, J.B. Kidd, G.J. Meyer, M. Baik, T. P. Yoon, J. Am. Chem. Soc. 141 (2019) 13625–13634.
[7] S. Fukuzumi, K. Ohkubo, F. D'Souza, J.L. Sessler, Chem. Commun. 48 (2012) 9801–9815.
[8] P. Jagadesan, S.R. Valandro, K.S. Schanze, Mater. Chem. Front. 4 (2020) 3649–3659.
[9] J.M. Gardner, M. Abrahamsson, B.H. Farnum, G.J. Meyer, J. Am. Chem. Soc. 131 (44) (2009) 16206–16214.
[10] L. Troian-Gautier, E.E. Beauvilliers, W.B. Swords, G.J. Meyer, J. Am. Chem. Soc 138 (2016) 16815–16826.
[11] S.A.M. Wehlin, L. Troian-Gautier, R.N. Sampaio, L. Marcélis, G.J. Meyer, J. Am. Chem. Soc. 140 (25) (2018) 7799–7802.
[12] P.D. Beer, P.A. Gale, Angew. Chemie Int. ed. English 40 (3) (2001) 486–516.
[13] P.D. Beer, F. Szemes, V. Balzani, C.M. Salà, M.G.B. Drew, S.W. Dent, M. Maestri, J. Am. Chem. Soc. 119 (1997) 11864–11875.
[14] L.H. Uppadine, M.G.B. Drew, P.D. Beer, Chem. Commun. (2001) 291–292.
[15] P.D. Beer, N.C. Fletcher, Polyhedron 8 (1996) 1339–1347.
[16] M.D. Turlington, L. Troian-Gautier, R.N. Sampaio, E.E. Beauvilliers, G.J. Meyer, Inorg. Chem. 57 (9) (2018) 5624–5631.
[17] M.D. Turlington, L. Troian-Gautier, R.N. Sampaio, E.E. Beauvilliers, G.J. Meyer, Inorg. Chem. 58 (2019) 3316–3328.
[18] H.J. Jang, S.L. Hopkins, M.A. Siegler, S. Bonnet, Dalt. Trans. 46 (2017) 9969–9980.
[19] A. Juris, V. Balzani, P. Belser, A. Zelewsky, von, Helv. Chim. Acta 64 (1981) 2175–2182.
[20] D.W. Thompson, A. Ito, T.J. Meyer, Pure Appl. Chem 85 (7) (2013) 1257–1305.
[21] R.L. Blakley, M.K. DeArmond, J. Am. Chem. Soc. 109 (1987) 4895–4901.
[22] P. Thordarson, Chem. Soc. Rev. 40 (2011) 1305–1323.
[23] D.B. Hibbert, P. Thordarson, Chem. Commun. 52 (2016) 12792–12805.
[24] J.N. Demas, G.A. Crosby, J. Phys. Chem. 75 (1971) 991–1024.
[25] S.W. Bigger, P.J. Watkins, B. Verity, Int. J. Chem. Kinet. 32 (2000) 473–477.
[26] H. Wang, S. Fang, G. Wu, Y. Lei, Q. Chen, H. Wang, Y. Wu, C. Lin, X. Hong, S. K. Kim, J.L. Sessler, H. Li, J. Am. Chem. Soc. 142 (2020) 20182–20190.
[27] L. Troian-Gautier, S.A.M. Wehlin, G.J. Meyer, Inorg. Chem. 57 (19) (2018) 12232–12244.
[28] G. Li, W.B. Swords, G.J. Meyer, J. Am. Chem. Soc. 139 (2017) 14983–14991.
[29] P.D. Beer, S.W. Dent, T.J. Wear, J. Chem. Soc., Dalt. Trans. (1996) 2341–2346.
[30] Y. Liu, A. Sengupta, K. Raghavachari, A.H. Flood, Chem 3 (2017) 411–427.
[31] J.M. Gardner, M. Abrahamsson, B.H. Farnum, G.J. Meyer, J. Am. Chem. Soc. 131 (2009) 16206–16214.
[32] K.C. Szeto, O.K. Kongshaug, S. Jakobsen, M. Tilset, K.P. Lillerud, Dalt. Trans (2008) 2054–2060.
[33] B. An, L. Zeng, M. Jia, Z. Li, Z. Lin, Y. Song, Y. Zhou, J. Cheng, C. Wang, W. Lin, J. Am. Chem. Soc. 139 (2017) 17747–17750.
[34] T. Hadda, H. Ben; Le Bozec, Polyhedron 7 (7) (1988) 575–577.
[35] K. Adamson, C. Dolan, N. Moran, R.J. Forster, T.E. Keyes, Bioconjug. Chem. 25 (2014) 928–944.
[36] R.M. O'Donnell, R.N. Sampaio, G. Li, P.G. Johansson, C.L. Ward, G.J. Meyer, J. Am. Chem. Soc. 138 (11) (2016) 3891–3903.
[37] A.M. Deetz, L. Troian-Gautier, S.A.M. Wehlin, E.J. Piechota, G.J. Meyer, J. Phys. Chem. A 125 (2021) 9355–9367.
[38] R. Argazzi, C.A. Bignozzi, T.A. Heimer, F.N. Castellano, G.J. Meyer, Inorg. Chem. 33 (1994) 5741–5749.
[39] B.N. Dimarco, R.M. O'Donnell, G.J. Meyer, J. Phys. Chem. C 119 (2015) 21599–21604.